IOP Publishing and International Atomic Energy Agency Nuclear Fusion

Nucl. Fusion **49** (2009) 085028 (10pp) doi:10.1088/0029-5515/49/8/085028

Impurity transport studies in NSTX neutral beam heated H-mode plasmas

L. Delgado-Aparicio[1], D. Stutman[1], K. Tritz[1], M. Finkenthal[1], S. Kaye[2], R. Bell[2], R. Kaita[2], B. LeBlanc[2], F. Levinton[3], J. Menard[2], S. Paul[2], D. Smith[2] and H. Yuh[3]

[1] The Johns Hopkins University, Department of Physics and Astronomy, Baltimore, MD 21218, USA
[2] Princeton Plasma Physics Laboratory, Princeton, NJ 08543, USA
[3] NOVA Photonics, Inc., Princeton, NJ 08543, USA

E-mail: delgapa@pha.jhu.edu

Received 22 January 2009, accepted for publication 15 June 2009
Published 22 July 2009
Online at stacks.iop.org/NF/49/085028

Abstract
The first experimental assessment of low-Z impurity transport in a neutral beam heated, high-confinement H-mode plasma sustained in a low-field, low-aspect ratio spherical tokamak, was performed at the National Spherical Torus Experiment (NSTX). The injected impurities penetrate to the core on a hundred millisecond time scale, indicating a low core particle diffusivity ($\lesssim 1\,\mathrm{m^2\,s^{-1}}$) in good agreement with the values predicted by neoclassical transport theory. In addition, a fixed q-profile magnetic field scan that showed reduced impurity penetration at high fields is also reported. This result suggests that anomalous ion particle transport associated with turbulent long-wavelength electrostatic instabilities must be largely suppressed in the NSTX core.

PACS numbers: 52.55.Fa, 52.55.Fi, 52.25.Vy

(Some figures in this article are in colour only in the electronic version)

1. Motivation

The understanding of impurity transport in a magnetically confined fusion (MCF) plasma is one of the challenges of current fusion research as the exhaust from high-power plasmas will ultimately strike and erode the material surfaces of the containment device. Both low-Z and high-Z materials are under consideration for the plasma facing components (PFCs) in a high-power fusion device, but each has technological hurdles that must be overcome. Low-Z materials typically have a higher erosion rate, but contribute less to radiated power losses with their accumulation in the plasma. Conversely, high-Z materials can better withstand the various erosion processes, but will radiate large amounts of power ($P_{\mathrm{rad}} \propto Z^2$) from the plasma if they accumulate to any substantial levels. Therefore, reducing the concentration of impurities towards the magnetic axis is important for mitigating the radiation losses and the fusion fuel dilution that can limit the achievable fusion power.

The spherical torus (ST) is a low-aspect ratio tokamak ($A = R_0/a < 1.5$) studied as an economical alternative to the conventional large-aspect ratio tokamaks ($A > 2.5$), because of its ability to sustain a high plasma pressure at significantly lower toroidal magnetic field [1–4], which translates directly to high beta (β is defined as the ratio of the plasma pressure to the magnetic field energy density ($\beta \equiv 2\mu_0\langle nk_{\mathrm{B}}T\rangle/B^2$)). One of the predicted benefits at low-aspect ratio is the reduction of the anomalous ion transport, important for the development of high-confinement H-mode plasmas. This reduced transport [5, 6] is generally attributed to the $\vec{E}\times\vec{B}$ shear stabilization of long-wavelength microinstabilities [7], the stability of high-n ballooning modes [8] or a strong stabilizing factor of turbulent drift modes given by $\nabla\beta$ [9]. To date, ST experimental impurity transport results have indicated neoclassical particle transport in the core ($D \lesssim 1.0\,\mathrm{m^2\,s^{-1}}$ for $\rho = r/a < 0.5$) of both the Current Drive Experiment Upgrade (CDX-U) ohmic discharges [10] and the National Spherical Torus Experiment (NSTX) low-confinement L-mode plasmas [5]. Such measurements were performed using intrinsic (carbon and oxygen) impurity profiles and neon injection, respectively.

Particle and impurity transport properties at low-aspect ratio remain important for extrapolation to next step ST devices such as CTF [4], and for comparison with the large-aspect ratio conventional tokamaks. This comparison with conventional tokamaks is done through the normalized gyro-radius ($\rho^* = \rho/a$); for the present experiments we have increased both the plasma current and the toroidal field as part of the fixed q-profile ion gyro-radius scan. This paper

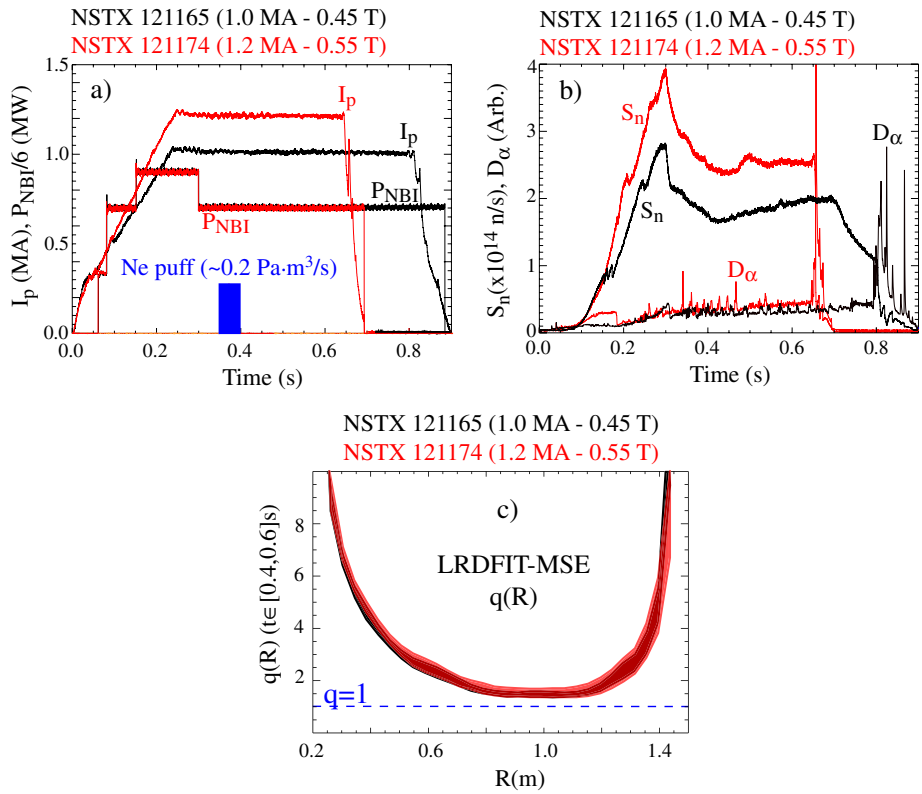

Figure 1. (*a*) Plasma current and NBI power, (*b*) neutron rate and D_α and (*c*) MSE-LRDFIT q-profile. (Colour online.)

describes the first results obtained from the first impurity transport experiments done in a neutral beam heated (NBI), high-confinement (H-mode) discharge in an ST configuration. In addition, results from a magnetic field and plasma current scan at fixed q-profile show that operation at higher toroidal field and plasma current reduced the impurity penetration significantly. The paper is organized as follows. Section 2 presents the description of the NSTX device, the experimental conditions and the diagnostics used for impurity transport measurements. An assessment of the transport experimental results and their comparison with transport and gyro-kinetic simulation codes is described in section 3, with the final remarks in section 4.

2. Impurity injections in NSTX H-mode plasmas

2.1. H-mode description

NSTX [1] is a low-aspect ratio ($R_0 \sim 85$ cm, $a \sim 65$ cm with an aspect ratio $A \geqslant 1.3$) spherical tokamak which operates with a toroidal magnetic field of 0.35–0.55 T; its internal walls are covered with carbon PFCs; thus carbon is the main impurity source. In the perturbative impurity transport experiments performed in NSTX H-modes, the external toroidal field (B_ϕ) and the plasma current (I_p) were varied simultaneously to observe transport and confinement effects at fixed $q_{95} \sim B_\phi/I_p$; the latter translates in a fixed q-profile as is shown below. The neon injection and resultant impurity transport measurements were performed under two different conditions: the lower-field ($I_p = 1.0$ MA, $B_\phi = 0.45$ T) and higher-field ($I_p = 1.2$ MA, $B_\phi = 0.55$ T) plasmas shown in figure 1. These H-modes had a tangential ($R_{tan} \sim 48.7$, 59.2 and 69.4 cm) deuterium beam injection power of $P_{NBI} \sim 4$–6 MW at 70–90 kV, with slowly evolving neutron rates of ~2.0 and 2.5×10^{14} neutrons s^{-1}, respectively (see figures 1(*a*) and (*b*)). At approximately $t \sim 300$ ms the third NBI source at 70 kV was turned off to avoid large type I edge localized modes (ELMs) that can affect both the thermal and particle transport; the other two NBI sources at 90 kV were on for the duration of the discharges. The smoothness in the neutron signals indicates that these H-modes had no core MHD as well as no fast-ion redistribution and/or anomalous fast-ion particle losses that could affect the impurity particle transport experiments; in this respect, the measured neutron rates agree well with the ones calculated by TRANSP, indicating no losses or redistribution of fast-ion density. The D_α signals correspond to small ELMs that have a negligible impact on the plasma stored energy. These plasmas were double-null diverted (DND), with average elongation (κ) and triangularity (δ) of the order of 2.25 and 0.6, respectively. Despite the differences in I_p and B_ϕ, the plasma shape and q-profile of the two discharges were well matched as shown in figure 1(*c*), largely due to the real-time control of the plasma boundary (the rtEFIT plasma control system [11]). The band of profiles shown in figure 1(*c*) corresponds to the envelope of time history profiles for the safety factor $q(R)$ during a time window of 200 ms. Operation at moderate β with a central safety factor $q > 1$ allows the avoidance of sawteeth, internal reconnection events and large ELMs, which could affect the magnitude and interpretation of the measured impurity transport coefficients.

The multi-point Thomson scattering (MPTS) electron density (n_e) and temperature (T_e) profiles shown in figure 2

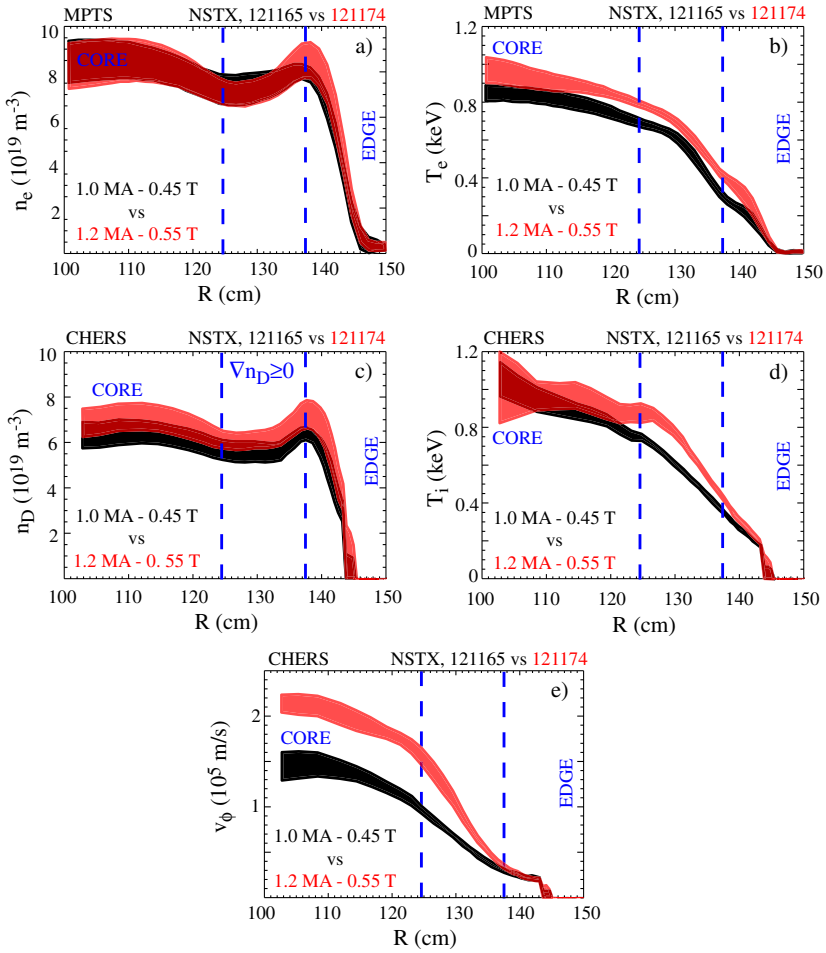

Figure 2. MPTS-spline and CHERS profiles for the low-field (in black, 1.0 MA, 0.45 T) and high-field (in red, 1.2 MA, 0.55 T) neon-seeded H-mode plasmas. The band of values for each condition corresponds to the envelope of time history profiles for a time window of 200 ms after the injection. (Colour online.)

are relatively broad, while the carbon charge exchange recombination spectroscopy (CHERS) ion temperature (T_i) profile is slightly more peaked. The deuterium density is obtained by subtracting the fully stripped carbon density from the Thomson scattering electron density diagnostic. The electron density 'ears' characteristic of both MAST and NSTX H-modes are located at approximately $R \sim 138$–140 cm, equivalent to $r/a \sim 0.8$. These 'ears' are indicative of an electron density build-up at the plasma boundary due to the carbon fuelling of the edge and the low levels of particle transport at the 'top' of the gradient region. Toroidal rotation is 40–70% higher in the case of the higher confinement regime inside $R < 130$ cm (see figure 2(*e*)) and will translate into broader shearing rate frequencies (as will be discussed below). The average plasma stored energy for the low-field shot was 220 kJ with $\beta_t \sim 14\%$ ($\beta_t \equiv 2\mu_0\langle nk_BT\rangle/B_t^2$, where B_t is the toroidal field) and a global energy confinement time (τ_E) of the order of ∼50 ms. Due to the higher electron and ion temperatures for the high-field case, both the τ_E and the plasma stored energies increased to 60 ms and 270 kJ, respectively with $\beta_t \sim 12\%$. These H-mode discharges were also characterized by $T_i/T_e > 1$ throughout the NSTX cross section, despite the fact that only about 30–40% of the NBI power was computed to heat the ions ($E_{NBI} \sim 90$ keV $\gg T_e$).

2.2. *Diagnostic description*

The perturbative impurity transport experiments used a transient neon puff injected from an outboard midplane port as an impurity particle source with a strong spectral signature in the soft x-ray range of 0.1–2.0 keV (see reference [5] and figure 3). The primary diagnostic used was the tangential multi-energy, optical (scintillator-based) soft x-ray (OSXR) array [12–17] depicted in figure 4. This instrument consists of three horizontal midplane rows of 16 channels, each viewing an overlapping plasma volume spanning from the outboard edge to just past the centre of the plasma midplane; the diagnostic time resolution is around 50–100 μs. Although this system was originally designed for fast electron temperature measurements (<0.1 ms) and MHD studies [14, 15], it is also filtered for energy bands covering the entire neon spectrum emitted from NSTX [15–17]. These SXR metallic foils are used to discriminate between the 0.9–1.3 keV line emission (e.g. from H- and He-like neon ions) mostly dominant in the peripheral plasma, and the enhanced continuum emission (from fully stripped neon ions) primarily from the inner plasma. Two 'synthetic' spectra are shown in figure 3; the first one (in black) shows the continuum radiation with the carbon and oxygen recombination edges as well as their characteristic line emission of a neon-free plasma. A small amount of neon

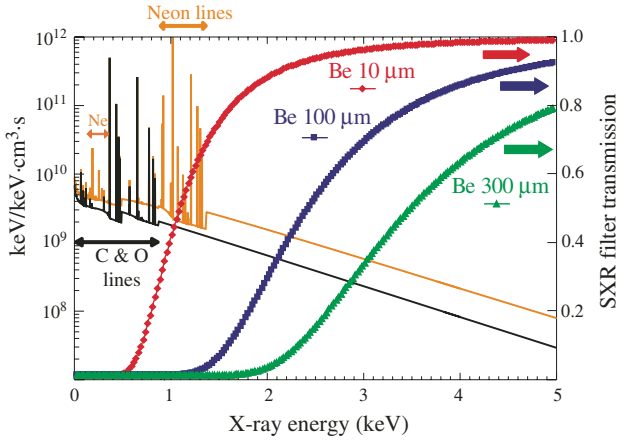

Figure 3. NSTX synthetic XUV spectra with deuterium, carbon and oxygen content (in black, $n_C/n_e \sim 5\%$ and $n_O/n_e \sim 0.5\%$) and neon-seeded plasma (in orange, $n_C/n_e \sim 5\%$, $n_O/n_e \sim 0.5\%$ and $n_{Ne}/n_e \sim 0.5\%$). The SXR filter transmission curves for 10, 100 and 300 μm beryllium SXR foils are overlaid in red, blue and green, respectively. (Colour online.)

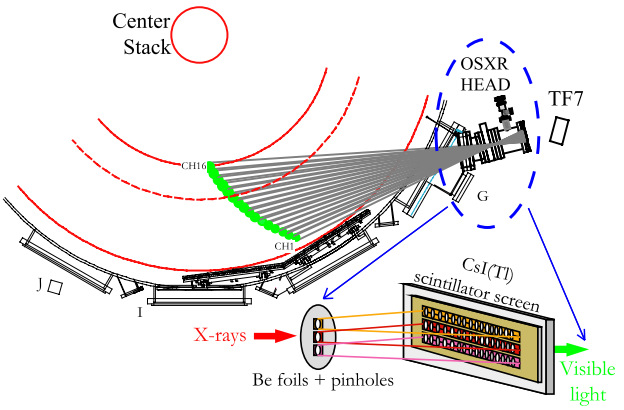

Figure 4. Tangential multi-energy optical (scintillator-based) SXR array; each of the three overlapping groups of 16 sightlines is equipped with a different beryllium filter (10, 100 and 300 μm, respectively) [13–17]. (Colour online.)

has been added to the atomic computation, thus obtaining the second spectrum (in orange). The latter shows the continuum enhancement over the neon-free plasma, the strong radiating Ne lines from 700 to 1300 eV as well as the neon recombination edge at ~1.4 keV; the impurity concentrations considered were of the order of $n_C/n_e \sim 5\%$, $n_O/n_e \sim 0.5\%$ and $n_{Ne}/n_e \sim 0.5\%$ for a plasma at an electron temperature and density of the order of ~1 keV and $\sim 5 \times 10^{19}$ m^{-3}, respectively. For a neon seeded plasma (see orange spectrum in figure 3), the signals obtained from the low-energy array filtered by a thin beryllium 10 μm foil (cutoff energy for 10% transmission, $E_{c,10\%} \sim 0.8$ keV) will be dominated by emission lines from the He- and H-like (Ne^{8+}, Ne^{9+}) neon charge states;
these atomic charge states are located primarily near the plasma boundary right after the injection ($r/a \gtrsim 0.6$) and also throughout NSTX cross section—depending on their transport properties—at later times. The contribution from the fully stripped Neon (Ne^{10+}) measured solely by the continuum enhancement on the other hand, is mostly from the central plasma that is imaged both by the inner (core) sightlines of the low-energy array and by all the medium- and high-energy detectors filtered with the thicker Be 100 μm ($E_{c,10\%} \sim 1.7$ keV) and 300 μm ($E_{c,10\%} \sim 2.4$ keV) foils; additional information on this filtering technique could be found in [14–17] and references therein.

The low- and medium-energy line-integrated signals obtained during the low-field (1.0 MA, 0.45 T) and high-field (1.2 MA, 0.55 T) H-modes are illustrated in figure 5. The black waveforms represent the SXR background measured in subsequent reproducible discharges, while the red signals are from the neon seeded plasma. The neon puff was injected at a rate of ~0.2 Pa m^3 s^{-1} within the time window of 350–400 ms as indicated by the shaded region. The experimental observations from the neon injection at low fields indicate a fast build-up of the impurity at the plasma edge with a subsequent, slower, impurity-build-up in the plasma core (see blue arrows in figures 5(*a*) and (*b*)). Late ($t \sim 700$ ms) in the discharge, this accumulation leads to strong peaking of the SXR emissivity profile and the triggering of a large (1,1) MHD mode in the core which flattens the T_e profile. As can be seen in figures 5(*c*) and (*d*), the penetration of impurities at high fields has been significantly reduced in comparison with the low-field H-modes, and the impurity-triggered MHD was also suppressed. The transport analysis will be restricted to the first 300 ms (~$6\tau_E$) after the initiation of the neon puff, a time long enough to study both the diffusive and convective transport coefficients; the MHD-dominated 'transport' of impurities has not been considered here and will be addressed in a future paper. The SXR contribution from the injected neon impurity charge states is obtained by first subtracting the intrinsic background using a reference (neon-free H-mode) reproducible discharge (signals in black), then reconstructing the radial emissivity profiles using a matrix-based Abel inversion technique [14]. The inversion of the SXR emissivity profile is sensitive to the derivative of the measured line-integrated brightness, therefore an appropriate smoothing of the data is generally required for the line-integrated experimental data and its associated noise. The smoothing and inversion procedure is as follows. First, the temporal resolution is reduced with a 1.0 ms averaging window. Then, a cubic spline smoothing procedure was used to process the line-integrated data prior to inversion using a smoothing parameter calculated from the rms noise of the signal. The degree of smoothing is such that the resultant function fits within the data uncertainty in the averaging window. Lastly, a matrix-based routine is used for Abel-inversion. This technique has been used in both tangential imaging of soft and hard x-rays [18] as well as for CHERS [19].

Figures 6(*a*), (*b*), (*d*) and (*e*) as well as 7(*a*), (*b*), (*d*) and (*e*) present the 2 ms time-averaged experimental neon SXR emissivities for the low-energy-Be 10 μm ($\varepsilon_{10\,\mu m} \propto n_{Ne^{8+}} + n_{Ne^{9+}}$) and medium-energy-Be 100 μm ($\varepsilon_{100\,\mu m} \propto n_{Ne^{10+}}$) arrays associated with the low- and high-field cases, respectively. A comparison between the edge and core signals in figures 6 and 7 also indicates that at higher plasma current and toroidal magnetic fields, the penetration of the impurities into the core of the plasma is substantially reduced, as demonstrated by the pile-up of neon density in the outer half of the plasma. The peaking of neon line emission at

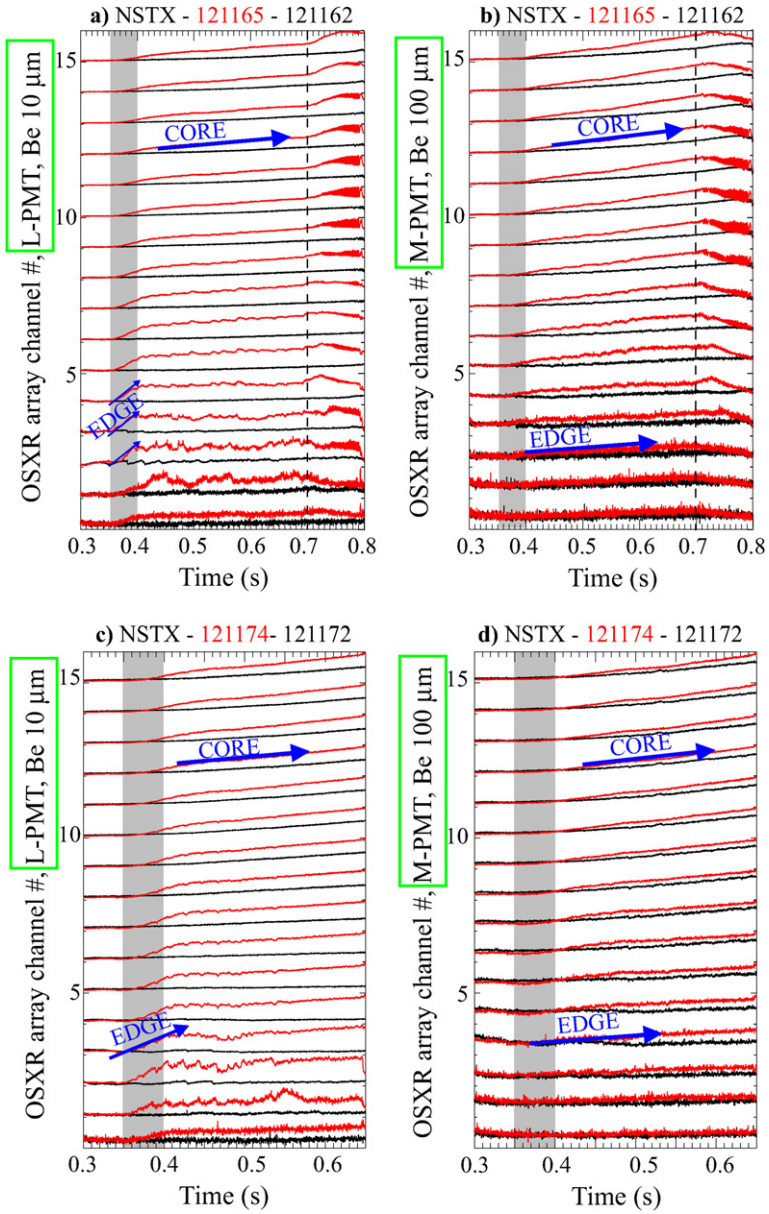

Figure 5. Multi-energy line-integrated SXR brightness signals obtained from reproducible background and neon seeded low-field (1.0 MA, 0.45 T, discharges 121162 and 121165) and high-field (1.2 MA, 0.55 T, discharges 121172 and 121174) H-mode plasmas. (Colour online.)

the outer plasma for the low-field case shown in figures 6(*a*) and (*b*), suggests that the Ne^{8+} and Ne^{9+} density peaking comes mainly from the region within the electron density 'ears' ($R \sim 130 \rightarrow 140$ cm) and also further inside (corresponding to $r/a \sim 0.6 \rightarrow 0.8$—see white dotted lines in the contour plot in figure 6(*a*)). However, for the high-field case, the corresponding peak of neon emission is located in the outer plasma identified by the density and temperature gradient region (on the peripheral side of the density ears, $R \sim 139 \rightarrow 142$ cm, $r/a \sim 0.8 \rightarrow 0.9$) even 300 ms after the initiation of the puff (see white dotted lines in the contour plot in figure 7(*a*)). A second observation using the same low-energy (Be d10 μm) response ($\varepsilon_{10\,\mu m} \propto n_{Ne^{8+}} + n_{Ne^{9+}}$, shown in figure 6(*b*)) is that its core signals have been reduced approximately by a factor of 3 in the high-field case (see figure 7(*b*)). Similarly, the core medium-energy SXR emissivity ($\varepsilon_{100\,\mu m} \propto n_{Ne^{10+}}$) has decreased by more than a factor of 2 in the high-field case (compare core emissivities from figures 6(*e*) and 7(*e*)), with profiles considerably narrower than its low-field counterpart. This emissivity analysis already demonstrates that the impurity build-up and its subsequent penetration to the core have been changed substantially when both the plasma current and the toroidal field were increased as part of the fixed q-profile ion gyro-radius (ρ^*) scan.

The time histories of the neon emissivity profiles after the injection were modelled using the one-dimensional (radial) and time-dependent MIST code [20] (see third column in figures 6 and 7). This simulation incorporates electron ionization, excitation and recombination processes for calculations of sinks and sources as well as ion particle transport coefficients

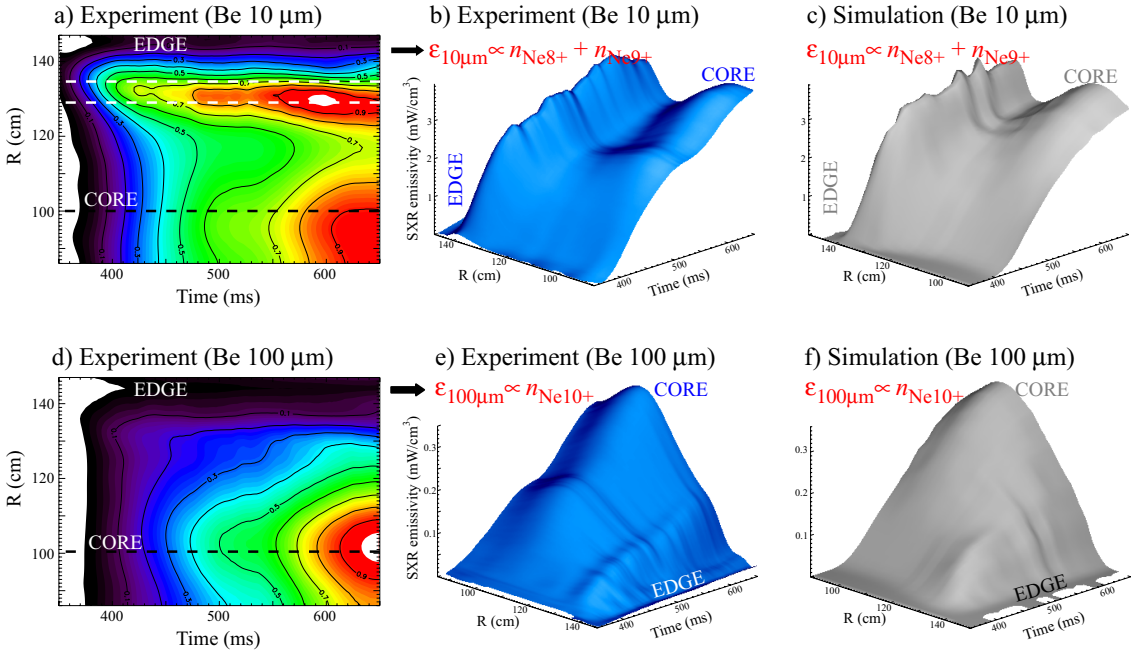

Figure 6. Experimental and multiple ionization stage transport (MIST) simulated neon SXR emissivity profiles filtered with Be 10 μm and Be 100 μm foils for the low-field (1.0 MA, 0.45 T) H-mode plasma. (Colour online.)

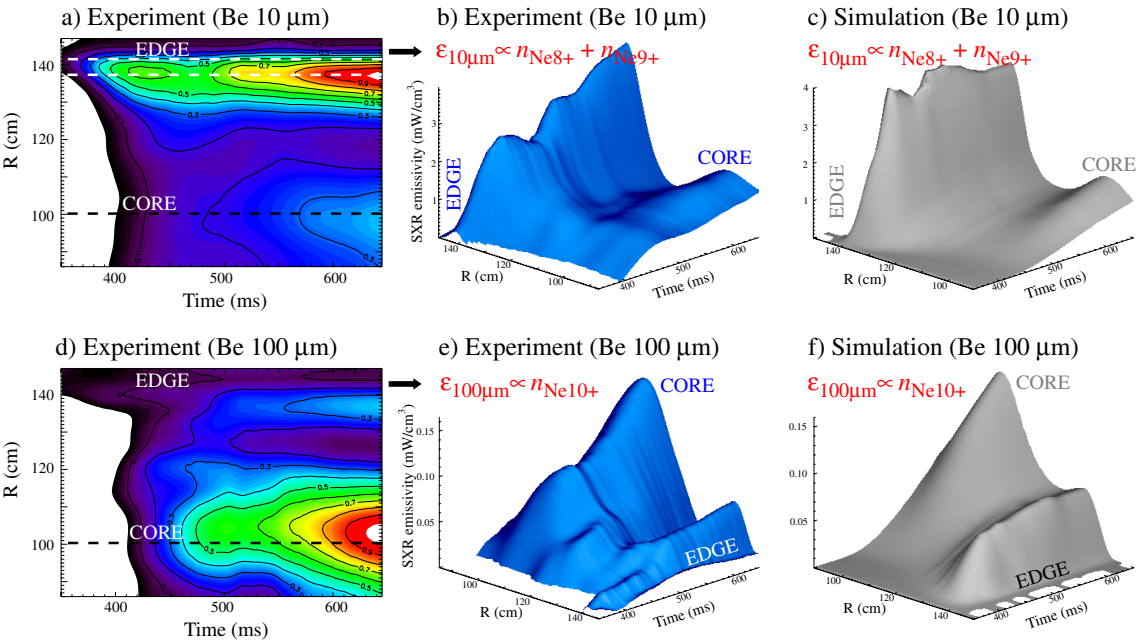

Figure 7. Experimental and MIST simulated neon SXR emissivity profiles filtered with Be 10 μm and Be 100 μm foils for the high-field (1.2 MA, 0.55 T) H-mode plasma. (Colour online.)

(see equations (1) and (2)).

$$\frac{\partial n_Z(r,t)}{\partial t} = -\nabla\cdot\Gamma_Z + [n_{(Z-1)}S_{(Z-1)\to Z} + n_{(Z+1)}S_{(Z+1)\to Z}] - n_Z[S_{Z\to(Z-1)} + S_{Z\to(Z+1)}], \quad (1)$$

$$\Gamma_Z(r,t) = -D_Z(r,t)\frac{\partial n_Z(r,t)}{\partial r} + n_Z(r,t)V_Z(r,t). \quad (2)$$

MIST was used to model the evolution of neon charge states using the experimental time histories of $n_e(R,t)$ and $T_e(R,t)$ shown in figure 2, and assuming external profiles of charge-independent neon diffusivity and convective velocity [5]. The MIST transport parameters were adjusted until a self-consistent solution matched both the SXR neon emissivity computed through MIST with the OSXR emissivity reconstructions (see figures 6 and 7), and the total radiated power with bolometer measurements. The neon-recycling coefficient used was $\lesssim$1.0 and the constraints for particle sources were imposed using the radiated power measured by a tangential midplane bolometer array (see figure 8 and [5]). Both the background-subtracted SXR emissivities filtered by

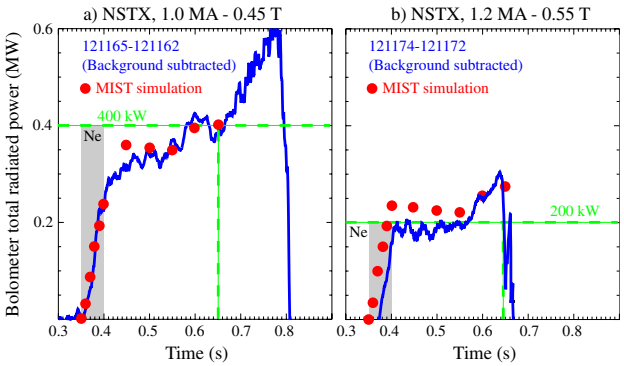

Figure 8. Background subtracted bolometer and MIST simulated neon radiated power for both the (*a*) low-field 1.0 MA, 0.45 T and (*b*) high-field 1.2 MA, 0.55 T H-mode plasmas. (Colour online.)

the Be 10 μm and Be 100 μm foils and the neon radiated power, fit within 10% and $\lesssim$20% of the values simulated by MIST, respectively. The somewhat larger discrepancy between the modelled and experimental bolometer radiated power is assumed to be due to the detector non-linear quantum efficiency at visible and near ultraviolet wavelengths [5].

3. Discussion of the impurity transport results

3.1. Particle diffusivity

The neon diffusion coefficients inferred from the MIST modelling are presented in figure 9(*a*) and decrease from a several m^2 s-1 in the outboard plasma to a fraction of m^2 s^{-1} inside r/a <0.8. The band of values represents the range of transport coefficients that reproduce the measured SXR emissivities in both spectral ranges within 10% or less [17]. As shown in [5], we find that the simultaneous inclusion of the multi-energy and the bolometer data, together with the time-dependent MIST modelling, puts a strong constraint in the determination of the transport coefficients at radii $r/a < 0.8$. It is interesting to note that for the gradient region ($R \gtrsim 137$ cm, $\rho \gtrsim 0.8$) the neon MIST diffusivity is greater than 1 m^2 s^{-1} and increases strongly with radius. The uncertainty in the particle diffusivity in the outer region is less constrained especially due to the small number of chords characterizing the gradient region of a high-β plasma. As concerns B-scaling, the experiment shows within error bars the $1/B^2$ neoclassical dependence inside r/a <0.7; this is an additional indication, together with the similarity of the experimental and neoclassical diffusion profiles, that the neon diffusion in the plasma core is neoclassical. Outside this radius although a change with B is observed, as further discussed peripheral MHD could also have played a role. For an assessment of neoclassical diffusivity in the NSTX H-mode, we have used the NCLASS code [21], which evaluates the neoclassical transport properties of a multi-species axisymmetric plasma of arbitrary aspect ratio, geometry and collisionality. This code has been adapted to NSTX toroidal geometry and uses as input the LRDFIT [22] magnetic flux surfaces reconstruction routine constrained by both the motional Stark effect (MSE) pitch angle diagnostic [23] and coil magnetic measurements at the edge. An NCLASS calculation of the (200 ms time-averaged)

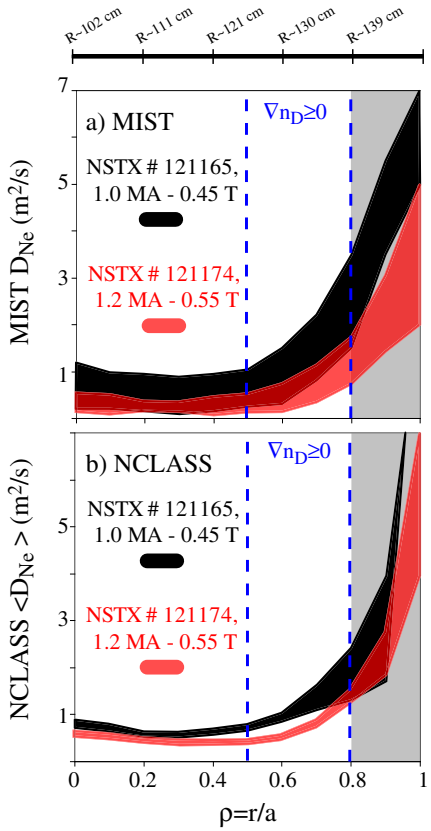

Figure 9. MIST and NCLASS neon diffusivities for the (*a*) low-field and (*b*) high-field H-mode plasmas. The shadowed grey regions were modelled over a higher uncertainty for both MIST and NCLASS. (Colour online.)

radial profiles for the particle diffusion coefficients is shown for comparison in figure 9(*b*).

The range of MIST inferred impurity diffusivities agree well with the neoclassical values calculated by NCLASS for r/a <0.7. Additionally, the NCLASS diffusivities in the outer plasma $r/a \gtrsim 0.8$ are also increasing with radius to a few m^2 s^{-1} due to the strong collisionality and rapidly increasing q^2 dependence of the Pfirsch–Schlüter diffusivity [24] (see equation (3)).

$$D_Z^{\rm PS} \approx \frac{\langle RB_\phi\rangle^2}{(\partial\psi/\partial r)^2}(\langle B^{-2}\rangle - \langle B^2\rangle^{-1})K_Z^{\rm PS}\frac{m_Z k_{\rm B} T_Z \nu_{Z,D}}{Z^2 e^2}. \quad (3)$$

For the large-aspect ratio circular approximation the product of the first two terms in the right-hand-side of equation (3) reduces to the neoclassical toroidal $2q^2/B^2_{\phi,0}$ enhancement over the cylindrical approximation. $K_Z^{\rm PS}$ is a function of the impurity strength factor $\alpha_Z = n_Z Z^2/n_D$ and the normalized main ion collisionality $\nu_D^* \epsilon^{3/2} = \nu_D/(v_{{\rm th},D}/Rq) \propto n_D/T_D^2$. For the NSTX densities and temperatures the main deuterium ions are well in the banana-plateau regime ($\nu_D^* \epsilon^{3/2} \ll 1$) and the neon concentrations (n_Z/n_D) are of the order of 10^{-3}, which in turn result in $K_Z^{\rm PS} \to 1$.

3.2. GS2 gyro-kinetic assessment

Impurity particle diffusivity of the order of the neoclassical values would indeed suggest that the anomalous ion particle transport associated with long-wavelength electrostatic

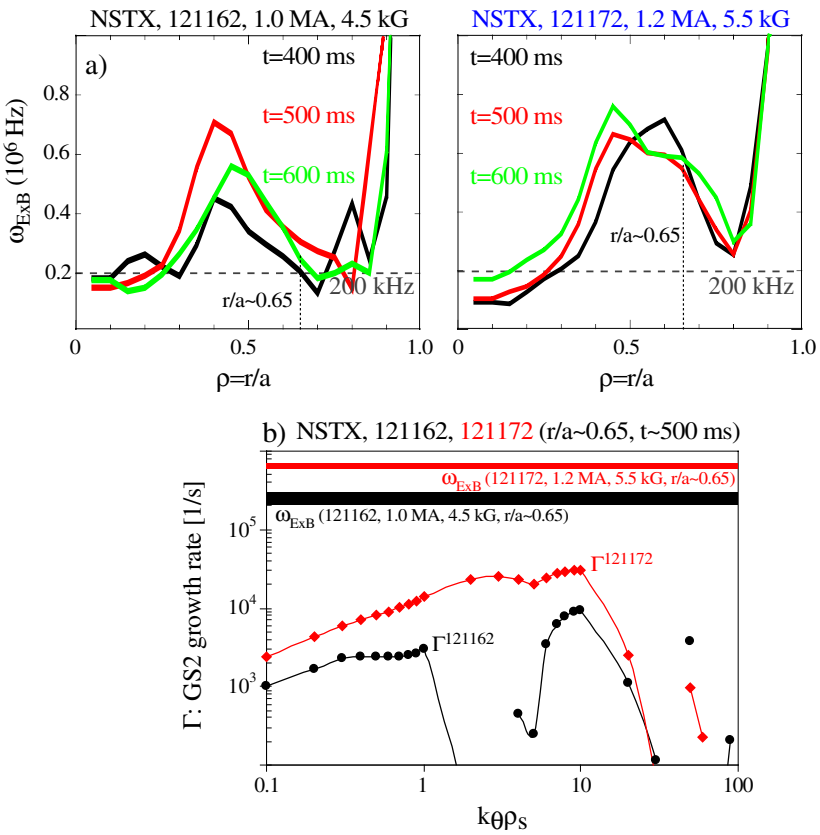

Figure 10. (*a*) NCLASS $\vec{E} \times \vec{B}$ shear and (*b*) GS2 growth rates. (Colour online.)

turbulence ($k_\theta \rho_s \lesssim 1$, with k_θ the poloidal wave number and ρ_s the ion sound–speed gyro-radius) must be largely suppressed in the NSTX core. We estimate that this happens because both the ion temperature gradient and the trapped electron modes (ITG/TEM) instabilities are likely stabilized by equilibrium $\vec{E} \times \vec{B}$ flow shear. The NCLASS $\vec{E} \times \vec{B}$ shear frequencies are shown in figure 10(*a*). We note that in comparison with previous results obtained in NSTX L-modes [5], these H-modes have shearing frequencies ∼2–3 times higher. The region of large $\vec{E} \times \vec{B}$ shear is also broader at high fields. For microstability analysis we performed calculations with the fully electromagnetic linear GS2 code [25], at multiple radial locations and different times for the background discharges.

The central electron density and electron and ion temperature in these plasmas are flat ($r/a \lesssim 0.4$, see figure 2), and thus the drive for core density and temperature gradient microinstabilities is absent. The GS2 microinstability growth rates for the low- and high-field plasmas at $r/a \sim 0.65$ are shown in figure 10(*b*); these growth rates indicate that although ITG/TEM modes could be present, they should be intrinsically stable ($1 < \Gamma_{\mathrm{ITG,TEM}} < 50$ kHz) due to the damping shearing rates ($\gtrsim$200 kHz, see band of values for shots 121162 (in black) and 121172 (in red)). In this respect we can safely assume that $\vec{E} \times \vec{B}$ shear can suppress the ITG/TEM modes. As $r/a \geqslant 0.7$, however, the ITG/TEM/ETG growth rates become on the order of or greater than the local shearing rate and no suppression will take place. While our experimental results indicate that $\vec{E} \times \vec{B}$ has an effect on transport, it is difficult to assess the role of the $\vec{E} \times \vec{B}$ velocity shear through comparisons with the linear GS2 predictions. Non-linear calculations [26] indicate that a large variability may exist in the level of velocity shear needed to suppress turbulence [$\omega_{\vec{E}\times\vec{B}} \gg \Gamma_{\max}$ instead of $\omega_{\vec{E}\times\vec{B}} > \Gamma_{\max}$].

3.3. Convective velocity discussion

The neon convective velocities inferred from the MIST modelling are presented in figure 11(*a*). For the high-field high-current case, an outward (positive) convective velocity of a few m s^{-1} in the region $r/a > 0.4$ is needed to model the low level of impurity accumulation inside the NSTX mid-radius and the hollow nature of the SXR emissivity profiles (see figure 7(*b*)). However, to model the peaking of neon density for the low-field H-mode, one needs an inward pinch velocity (see SXR emissivity peaking at the core in figure 6). The Pfirsch–Schlüter convective velocity is a strong function of Z as shown in equation (4); H_Z^{PS} is also a function of α_Z and the main ion $\nu_D^* \epsilon^{3/2}$.

$$V_Z^{\mathrm{PS}} \approx D^{\mathrm{PS}} Z \left(\frac{\mathrm{d} \ln n_D}{\mathrm{d}r} + \frac{H_Z^{\mathrm{PS}}}{K_Z^{\mathrm{PS}}} \frac{\mathrm{d} \ln T_D}{\mathrm{d}r} \right). \qquad (4)$$

At small impurity concentrations and a reduced deuterium collisionality ($\nu_D^* \epsilon^{3/2}$), the function H_Z^{PS} can change sign therefore modifying the contribution towards the convective velocity from the ion temperature gradient (see equation (4) and [24]). It is through this dependence on the plasma profiles that in the presence of a weak ion density gradient and a strong ion temperature gradient, the impurity density profiles may become hollow thus shielding the plasma core from unwanted

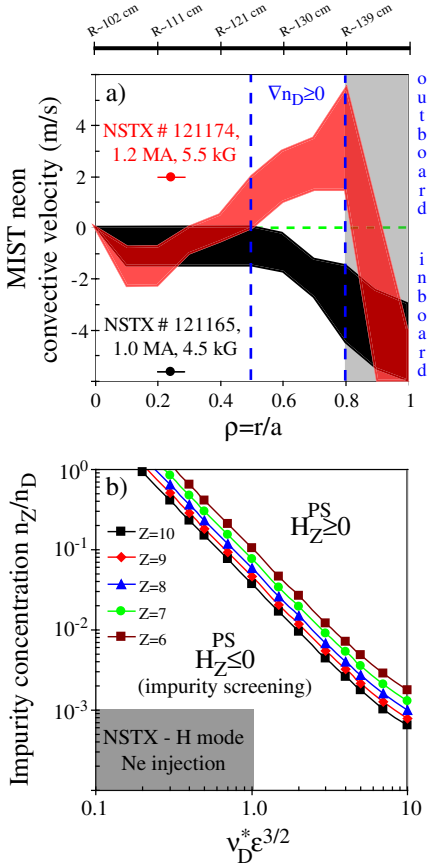

Figure 11. (*a*) MIST convective velocities inferred from the modelling for the low-field and high-field H-mode plasmas and (*b*) the sign of the neoclassical function H_Z^{PS} in $n_Z/n_D - \nu_D^* \epsilon^{3/2}$ space. (Colour online.)

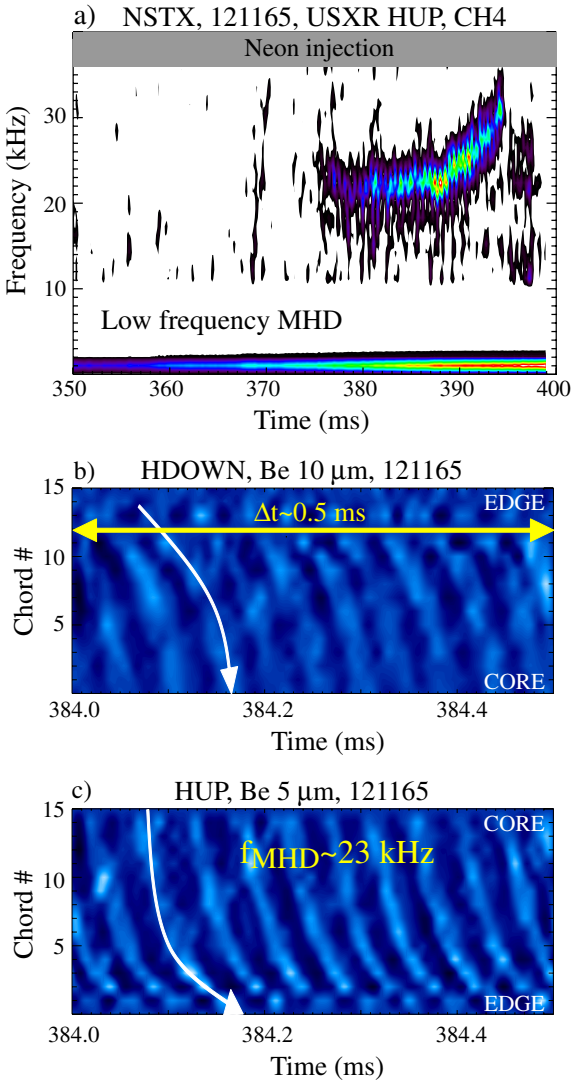

Figure 12. (*a*) Frequency spectrogram of the USXR data. A coherent ~22 kHz MHD mode structure for a peripheral magnetic island observed in the low-field shot during the neon build-up is imaged using the multi-energy horizontal USXR arrays filtered with the (*b*) Be 10 μm and (*c*) 5 μm foils. (Colour online.)

impurities. Although the steeper ion temperature gradient in the outer half of the plasma of the high-field discharge ($125 < R < 139$ cm, $0.5 < r/a < 0.8$) is more favourable for the screening of impurities in the higher-field case over the one at lower fields, the parameter space defined by n_Z/n_D and $\nu_D^* \epsilon^{3/2}$ (shown in figure 11(*b*)), indicates that both high- and low-field H-modes should have $H_Z^{PS} < 0$, resulting in a positive (radially outwards) convective velocity. For NSTX $\nu_D^* \epsilon^{3/2} < 1$ and $n_Z/n_D \sim 10^{-3}$, this function can be approximated as $H_Z^{PS} \to -1/2$.

Tentatively, we attribute the high density of neon and the needed (anomalous) negative pinch velocity (for the low-field H-mode) at the outer plasma to either the presence of a low-amplitude MHD island located in the plasma gradient region during the time of the neon injection or to the incomplete shear suppression of drift-wave-like instabilities at outer radii ($r/a \sim$ 0.7–0.9). The frequency spectrogram of a poloidal diode-based ultra soft x-ray (USXR) array [5] sightline is depicted in figure 12(*a*). The low-frequency 0.8–1.5 kHz MHD activity is common to both the low-field and the high-field H-modes; however, the coherent ~23 kHz MHD peripheral structure is only present on the low-field H-modes within the time of the neon gas puff; this high-m and $n = 1$ magnetic island observed during the neon build-up has been imaged by the multi-energy USXR array using Be 10 μm and 5 μm ($E_c \sim 0.6$ keV) foils and is shown in figures 12(*b*) and (*c*). This magnetic island located in between the plasma gradient region and mid-radius might have enhanced the penetration of impurities. The change in the sign of the convective velocity can also be due to the weaker shear suppression at low fields (see figure 10 and compare with wider $\vec{E} \times \vec{B}$ shear rates at high field) and the presence of drift-wave electrostatic ITG/TEM modes at the outer plasma [27–31]; experimental findings of neoclassical diffusivity with anomalous convective velocity have also been reported in high-aspect ratio tokamaks (see [28] and references therein). Therefore, the penetration of impurities for the low-field H-mode caused either by incomplete shear suppression at outer radii ($r/a \sim$ 0.6–0.9) during the entire discharge, or the presence of MHD activity within the time of the gas puff, could reflect in the higher density of neon and thus in the MIST simulation, as a substantial anomalous inward convective velocity.

4. Summary

We have reported the first experimental assessment of low-Z impurity transport in a neutral beam heated, high-confinement H-mode plasma in a low-aspect ratio spherical tokamak. The calculated core particle diffusivities found are in good agreement with the turbulence-free nature of the neoclassical transport. The usually large peripheral ($r/a > 0.8$) particle diffusivity in the NSTX H-mode seems to be due to the Pfirsch–Schlüter neoclassical transport associated with the high $q \approx 6$–10 value, high ion density ($\sim$6–7 $\times$ 10^{19} m^{-3}) and low ion temperature ($\sim$200 eV). Both the impurity build-up and its subsequent penetration to the core were changed substantially when the plasma current and the toroidal field were increased as part of the fixed q-profile scan. This result suggests that anomalous ion particle transport associated with turbulent long-wavelength electrostatic instabilities must be largely suppressed in the NSTX core. Additional experiments should be conducted in order to independently vary the q-profile and the plasma rotation for determining single parameter (I_p, B_ϕ) transport trends. An assessment of a turbulent pinch velocity (at an outer radii, for example the gradient region) associated with ITG and TEM modes for NSTX plasmas is underway.

Acknowledgments

The authors would like to acknowledge the assistance of D. McCune, E.A. Feibush and R.G. Andre of the PPPL Computational Plasma Physics Group and that of the technical and engineering teems at both The Johns Hopkins University and PPPL. This work was supported by the United States DoE grant No DE-FG02-99ER5452 at The Johns Hopkins University and PPPL DoE contract No DE-AC02-76CH03073.

References

[1] Ono M. *et al* 2000 *Nucl. Fusion* **40** 557
[2] Menard J.E. *et al* 1997 *Nucl. Fusion* **37** 595
[3] Jardin S.C. *et al* 2003 *Fusion Eng. Des.* **65** 165
[4] Peng Y.-K.M. *et al* 2005 *Plasma Phys. Control. Fusion* **47** B263
[5] Stutman D. *et al* 2003 *Phys. Plasmas* **10** 4387
[6] Kaye S. *et al* 2007 *Phys. Rev. Lett.* **98** 175002
[7] Kotschenreuther M. *et al* 2000 *Nucl. Fusion* **40** 677
[8] Rewoldt G. *et al* 1996 *Phys. Plasmas* **3** 1667
[9] Bourdelle C. *et al* 2003 *Phys. Plasmas* **10** 2881
[10] Soukhanovskii V.A. *et al* 2003 *Plasma Phys. Control. Fusion* **44** 2239
[11] Gates D. *et al* 2006 *Phys. Plasmas* **13** 056122
[12] Delgado-Aparicio L. *et al* 2004 *Rev. Sci. Instrum.* **75** 4020
[13] Delgado-Aparicio L. *et al* 2007 *Appl. Opt.* **46** 6069
[14] Delgado-Aparicio L. *et al* 2007 *J. Appl. Phys.* **102** 073304
[15] Delgado-Aparicio L. *et al* 2007 *Plasma Phys. Control. Fusion* **49** 1245
[16] Delgado-Aparicio L. *et al* 2007 *Proc. 34th EPS Conf. on Plasma Physics (Warsaw, Poland)* vol 31F (ECA) P-2.050
[17] Delgado-Aparicio L. 2007 Novel soft x-ray diagnostic techniques for the study of particle transport phenomena in magnetically confined fusion plasmas *PhD Thesis Dissertation* The Johns Hopkins University, USA
[18] Bell R.E. 1995 *Rev. Sci. Instrum.* **66** 558
[19] Bell R. 1997 *Rev. Sci. Instrum.* **68** 1273
[20] Hulse R. 1983 *Nucl. Technol. Fusion* **3** 259
[21] Houlberg W. *et al* 1997 *Phys. Plasmas* **4** 3320
[22] Menard J. 2007–2009 private communication Princeton Plasma Physics Laboratory (PPPL)
[23] Levinton F. *et al* 2007 *Phys. Plasmas* **14** 056119
[24] Dux R. *et al* 1999 *Nucl. Fusion* **39** 1509
[25] Kotschenreuther M. *et al* 1995 *Comput. Phys. Commun.* **88** 128
[26] Waltz E.R. *et al* 2002 *Phys. Plasmas* **9** 1938
[27] Garbet X. *et al* 2003 *Phys. Rev. Lett.* **91** 035001
[28] Guirlet R. *et al* 2006 *Plasma Phys. Control. Fusion* **48** B63
[29] Angioni C. *et al* 2006 *Phys. Rev. Lett.* **96** 095003
[30] Dubuit N. *et al* 2007 *Phys. Plasmas* **14** 042301
[31] Angioni C. *et al* 2007 *Plasma Phys. Control. Fusion* **49** 2027